Batteries & Supercaps

Research Article
doi.org/10.1002/batt.202400123

Chemistry Europe
European Chemical Societies Publishing

www.batteries-supercaps.org

Enhanced High Voltage Stability of Spinel-Type Structured $LiNi_{0.5}Mn_{1.5}O_4$ Electrodes: Targeted Octahedral Crystal Site Modification

Jinshuo Zou,[a] Gemeng Liang,*[a] Shilin Zhang,[a] Lars Thomsen,[b] Yameng Fan,[c]
Wei Kong Pang,[c] Zaiping Guo,[a, c] and Vanessa K. Peterson*[c, d]

High-voltage spinel-type structured $LiNi_{0.5}Mn_{1.5}O_4$ (LNMO) shows promise as a next-generation high-energy-density lithium-ion battery cathode material, however, capacity decay on extended cycling hinders its widespread adoption, underscoring an urgent need for further development. In this work, we introduce Zn at octahedral 16*c* crystal sites in LNMO with $Fd\bar{3}m$ space group to improve rate capability and reduce the rapid capacity decay otherwise experienced during extended cycling. The current work resolves the detailed influence of isolated modification at octahedral 16*c* crystal sites, unveiling the mechanism for these performance improvements. We show that occupation of Zn at previously empty 16*c* sites prevents the migration of Ni/Mn to adjacent 16*c* sites, eliminating transformation to a rock-salt type structured $Ni_{0.25}Mn_{0.75}O_2$ phase above 4.8 V, preventing structure degradation and suppressing voltage polarization. This study provides insights into the fundamental structure-function relationship of the LNMO battery cathode, pointing to pathways for the crystal structure engineering of materials with superior performance.

Introduction

Transportation electrification is critical in a societal low-carbon energy transition. Lithium-ion batteries (LIBs) are the main power supply for electric vehicles (EVs), and in comparison to the internal combustion engine, EVs suffer from limited driving range, originating from the limited energy densities of LIB cathodes.[1] Various high-energy battery cathode materials have been explored to increase LIB energy density, with the high-voltage spinel-type structured $LiNi_{0.5}Mn_{1.5}O_4$ (LNMO) materials regarded as promising cathode candidates for next-generation LIBs, enabling a battery energy density of ~650 Wh kg^{-1} with a low fabrication cost and minor environmental impact.[2]

Prior to their commercialization and potential widespread adoption in high-energy applications, performance issues of LNMO cathodes, including serious battery capacity decay, must be addressed.[3] Poor cycle stability and consequential short service life of LNMO is known to originate from crystal structure instability, notably during high voltage operation, ultimately limiting battery energy density.[4] In detail, the LNMO structure with $Fd\bar{3}m$ space group symmetry undergoes a solid-solution reaction until 4.8 V, beyond which the Ni^{4+}/Ni^{3+} redox couple contributes to two-phase reactions that involve phase boundary movement and stress, leading to electrode cracking, capacity loss, and ultimately rapid battery capacity decay.[5]

Elemental substitution in the LNMO structure with $Fd\bar{3}m$ space group symmetry has been widely explored to improve structure stability, with the inclusion of Ti shown to improve electrochemical performance, and the partially filled *d* orbitals of Fe^{3+} and Cr^{3+} leveraged to improve LNMO performance through their inclusion in the structure.[6] Despite these performance improvements, few studies have sought to understand the fundamental relationship between the LNMO structure and performance as a cathode, limiting the progress of materials design towards high-performance applications. In this work, we build on our previous work investigating the structure-function relationship of LNMO to unveil in detail the crystallographic-site-specific engineering of LNMO to address structural instability at high voltage.[7] Our previous results show that modification at both tetrahedral 8*a* and octahedral 16*c* sites,[7a] as well as at both octahedral 16*c* and 16*d* sites,[7b,c] in the $Fd\bar{3}m$ space group structure, enhance structure stability and resolve the rapid capacity decay during cycling. The current work resolves the detailed influence of isolated modification at 16*c* sites, unveiling the mechanism for structural stability enhancement for the first time.

---

[a] Dr. J. Zou, Dr. G. Liang, Dr. S. Zhang, Prof. Z. Guo
School of Chemical Engineering, The University of Adelaide, Adelaide, SA 5005, Australia
E-mail: gemeng.liang@adelaide.edu.au

[b] Dr. L. Thomsen
Australian Synchrotron, Australian Nuclear Science and Technology Organisation, Melbourne, VIC, Australia

[c] Dr. Y. Fan, Prof. W. K. Pang, Prof. Z. Guo, Prof. V. K. Peterson
Faculty of Engineering, Institute for Superconducting & Electronic Materials, University of Wollongong, Wollongong, NSW, Australia

[d] Prof. V. K. Peterson
Australian Centre for Neutron Scattering, Australian Nuclear Science and Technology Organisation, Sydney, NSW, Australia
E-mail: vanessa.peterson@ansto.gov.au

Supporting information for this article is available on the WWW under https://doi.org/10.1002/batt.202400123

Herein, we report the effects of 16*c* site engineering of LNMO electrodes on the mechanistic behaviour and electrochemical performance of LNMO within LIBs. In the unmodified LNMO structure with $Fd\bar{3}m$ space group symmetry, octahedral 16*c* sites are empty.[8] In this work we introduce Zn with a relatively large ionic radius (0.74 Å) to occupy these normally vacant 16*c* sites,[9] with the modified material having improved battery cycle stability with a capacity retention of 77% after 1000 cycles at 1 C (1 C = 147 mA g^{-1}), alongside enhanced rate performance. We use *in operando* synchrotron-based X-ray powder diffraction (SXRPD) to confirm that Zn at 16*c* sites acts as structural pillars to stabilize the structure and prevent two-phase reaction at high voltage. Near-edge X-ray absorption fine structure spectroscopy (NEXAFS) experiments confirm modification to the state of Mn and O in LNMO at the fully charged state by the inclusion of Zn in the structure. This work sheds light on the importance of a fundamental understanding of the structure-function relationship of battery materials in the successful design of high-performance high-voltage spinel-type structured cathodes for next-generation LIBs.

Results and Discussion

The nominal composition $LiNi_{0.5}Mn_{1.45}Zn_{0.05}O_4$ of the modified active material (Zn-LNMO) in which Zn is 1.67 atomic % of cations is in good agreement with the ~1.9% determined from inductively coupled plasma mass spectrometry (ICP-MS). The morphology of unmodified LNMO and Zn-LNMO materials was investigated using scanning electron microscopy (SEM, Figure 1a and 1b). A similar irregular polyhedral morphology is found in both samples, showing that the introduction of Zn

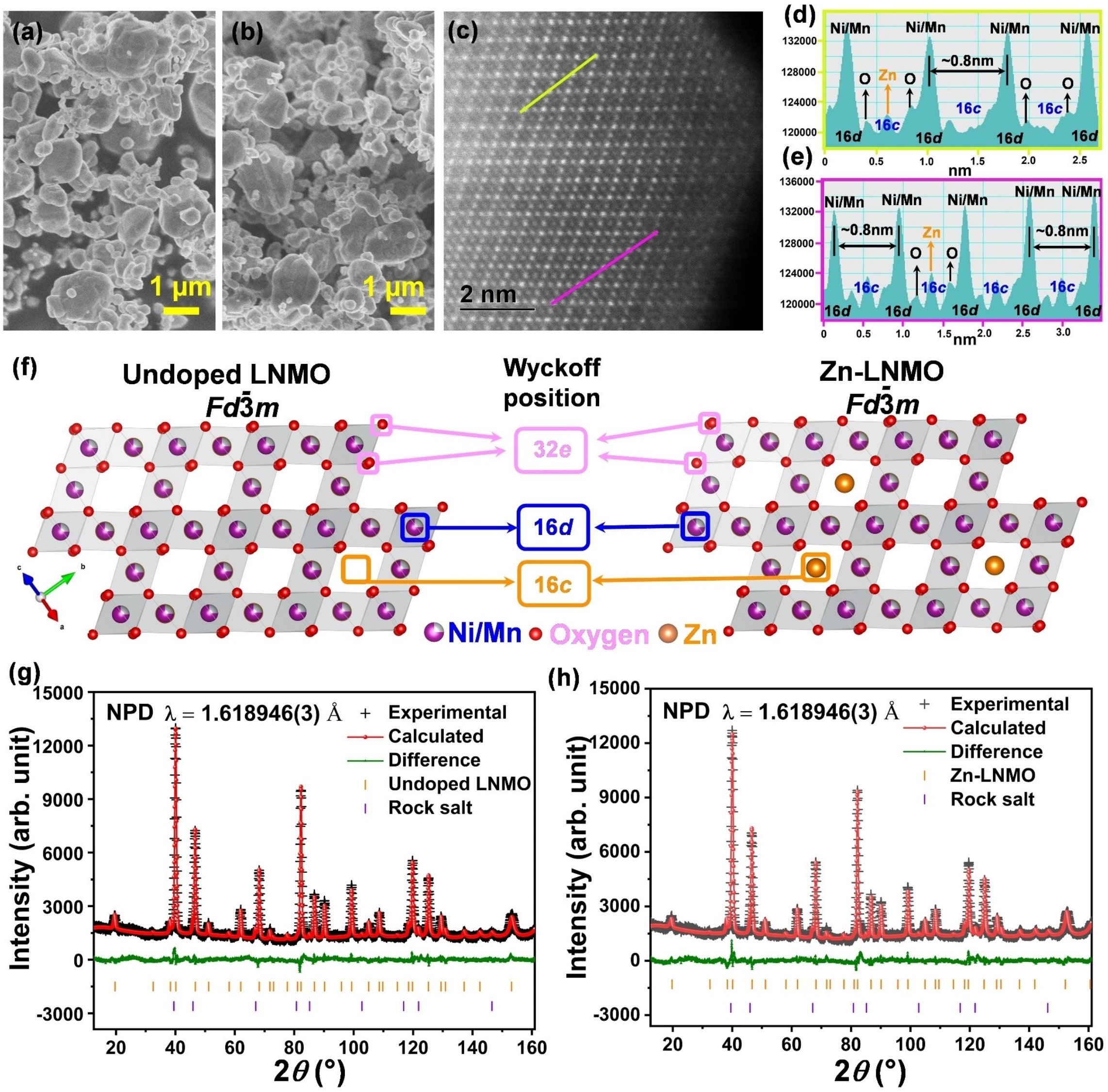

Figure 1. SEM images of (a) unmodified LNMO and (b) Zn-LNMO; (c) HAADF STEM image of the near-surface region of Zn-LNMO with corresponding line profile intensity along (d) light green and (e) purple line in (c); (f) schematic of the unmodified LNMO and Zn-LNMO crystal structure with color coded Wyckoff positions, and with Li excluded for clarity. Rietveld refinement profiles using NPD data of (g) unmodified LNMO with a weighted profile R-factor (R_{wp}) = 4.62% and goodness of fit (GOF) = 1.83, and (h) Zn-LNMO with R_{wp} = 5.06% and GOF = 2.04.

into the LNMO does not modify the material morphology. Aberration-corrected scanning transmission electron microscopy (STEM) was performed in high-angle annular dark-field (HAADF) mode, with the results shown in Figure 1c and S1. In these data, only relatively heavy elements such as Ni, Mn, and Zn, can be observed, and are seen as small bright dots.[10] HAADF STEM images (Figure 1c and S1b) along the [110] direction were recorded as per previous work, revealing characteristic diamond shaped arrangements of higher intensity in both samples, confirming the spinel-type structure of the materials.[7b,c,8,11] Additional intensity in the centre of these diamond shaped arrangements is seen in Zn-LNMO (Figure 1c), corresponding to the atomic occupation of 16*c* sites.[8] Line profile intensity of the HAADF STEM image (Figure 1d and 1e) confirms the existence of atoms at 16*c* sites, absent in the unmodified LNMO (Figure S1c). Rietveld refinement of structural models for unmodified LNMO and Zn-LNMO in which Ni and Mn share octahedral 16*d* sites, O occupies 32*e* sites, and Zn occupies octahedral 16*c* sites in Zn-LNMO (as shown schematically in Figure 1f) was carried out against neutron powder diffraction (NPD) data for both samples, and refinement profiles are shown in Figure 1g and 1h with refinement results tabulated in Table S1. Zn-LNMO is found to have a larger lattice parameter ($a = 8.1847(3)$ Å) than the unmodified LNMO ($a = 8.1761(2)$ Å), further confirming the inclusion of Zn in the crystal structure. A small amount of a rock-salt type structured phase was found in both materials and is ignored in the following discussion given the very low amount.

The structure-function relation of Zn-LNMO and unmodified LNMO was investigated using *in operando* SXRPD, and data shown as a contour plot with intensity in colour alongside the corresponding voltage in Figure 2. The diffraction peaks at approximately 8.35°, 16.05°, and 25.3° in 2θ correspond to the 111, 311, and 511 reflections of the $Fd\bar{3}m$ space group structure, respectively.[7c] Of these reflections, the 111 reflection has the strongest intensity, and in the unmodified LNMO (Figure 2a) this reflection shifts gradually to higher 2θ during charge from open circuit voltage (OCV) to approximately 4.7 V, indicating a solid solution behavior with contraction of the lattice parameter during Li extraction. After approximately 4.7 V, the 111 reflection amplitude abruptly drops and the width broadens. When the operating voltage approaches 4.8 V, a new reflection at approximately 8.52° appears, which can be indexed to the 111 reflection of the rock-salt type structured $Ni_{0.25}Mn_{0.75}O_2$

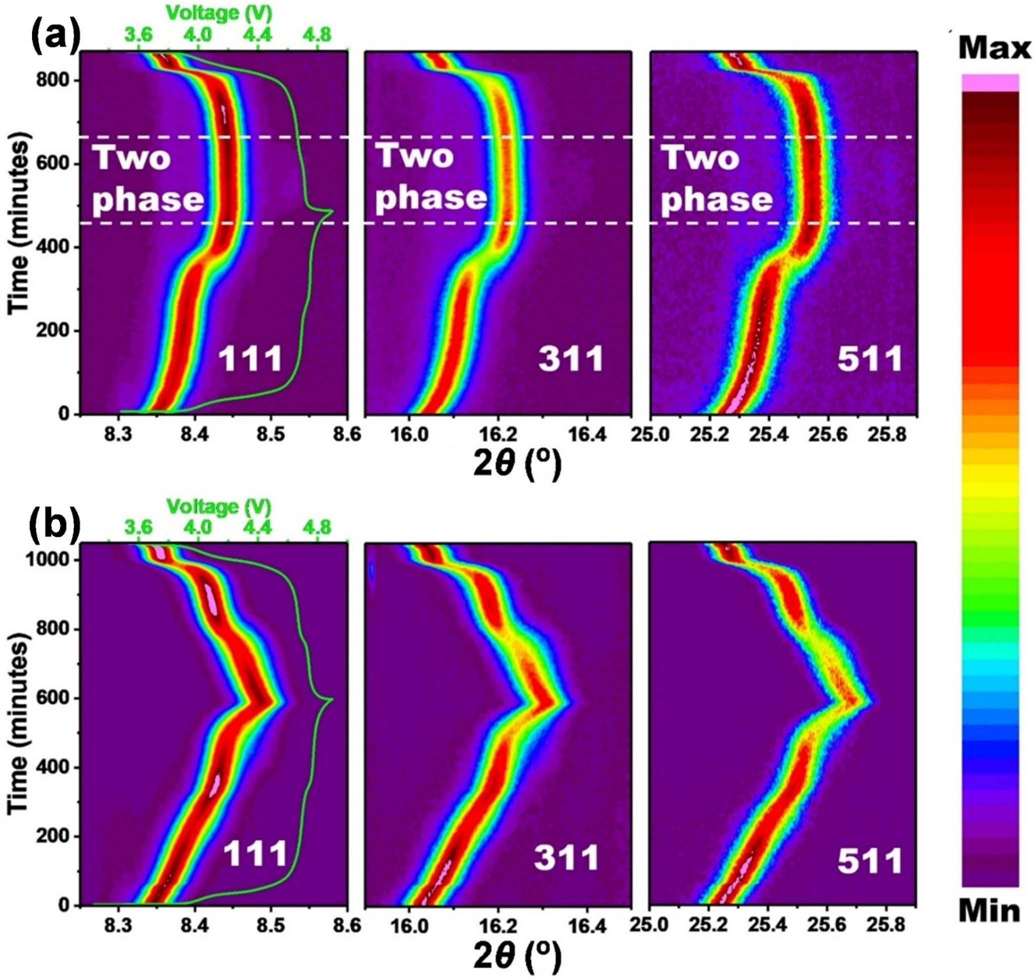

Figure 2. *In operando* SXRPD data shown as a contour plot with intensity in colour along with the corresponding voltage, in select 2θ regions showing the 111 (left), 311 (middle), and 511 (right) reflections of the $Fd\bar{3}m$ space group structure for (a) unmodified LNMO and (b) Zn-LNMO.

phase, indicating a two-phase reaction within the active materials.[4a,7b] This two-phase reaction induces intergranular stress that results in cathode particle cracking and pulverization, ultimately leading to active material loss and short cycle life.[12] The two-phase reaction persists until discharge to approximately 4.65 V where the LNMO 111 reflection returns to lower 2θ corresponding to the reinsertion of Li into the structure. In contrast, Zn-LNMO experiences a solid-solution reaction throughout the cycle, as evidenced by the continuous shift of the 111 reflection to higher 2θ (Figure 2b) during charge and back during discharge, without the appearance of the $Ni_{0.25}Mn_{0.75}O_2$ 111 reflection. The absence of a two-phase reaction in Zn-LNMO is attributed to the occupation of 16*c* octahedral sites by Zn, which serve as structural pillars within spinel-type structure that impede the migration of Ni or Mn to adjacent empty 16*c* sites, avoiding the initiation of a two-phase reaction.

Figure 3 compares the electrochemical performance of batteries containing each cathode material, with cyclic voltammetry (CV) data of unmodified LNMO and Zn-LNMO shown in Figure 3a and 3b, respectively. At a scan rate of 0.1 mV/s, both samples exhibit a weak anodic feature peak A at approximately 4.0 V, corresponding to the Mn^{3+} to Mn^{4+} transformation.[13] Anodic feature peak B and C are attributed to the Ni^{2+} to Ni^{3+} (at ~4.7 V) and Ni^{3+} to Ni^{4+} (4.8 V) transitions, respectively.[14] Doubling the scan rate to 0.2 mV/s causes peaks B and C to merge into a single broad feature in unmodified LNMO, while these features arising from the Ni^{2+}/Ni^{3+} and Ni^{3+}/Ni^{4+} redox couples remain discernible in Zn-LNMO.

Zn-LNMO and unmodified LNMO deliver an initial battery capacity of ~127 and ~113 mAh g^{-1} at 1 C, respectively, dropping to 98 mAh g^{-1} (77 % retention) and 70 mAh g^{-1} (62 % retention) after 1000 cycles (Figure 3c). Corresponding charge/discharge curves at the 5th and 1000th cycle are shown in Figure 3d. The electrochemical plateau at approximately 4.7 V

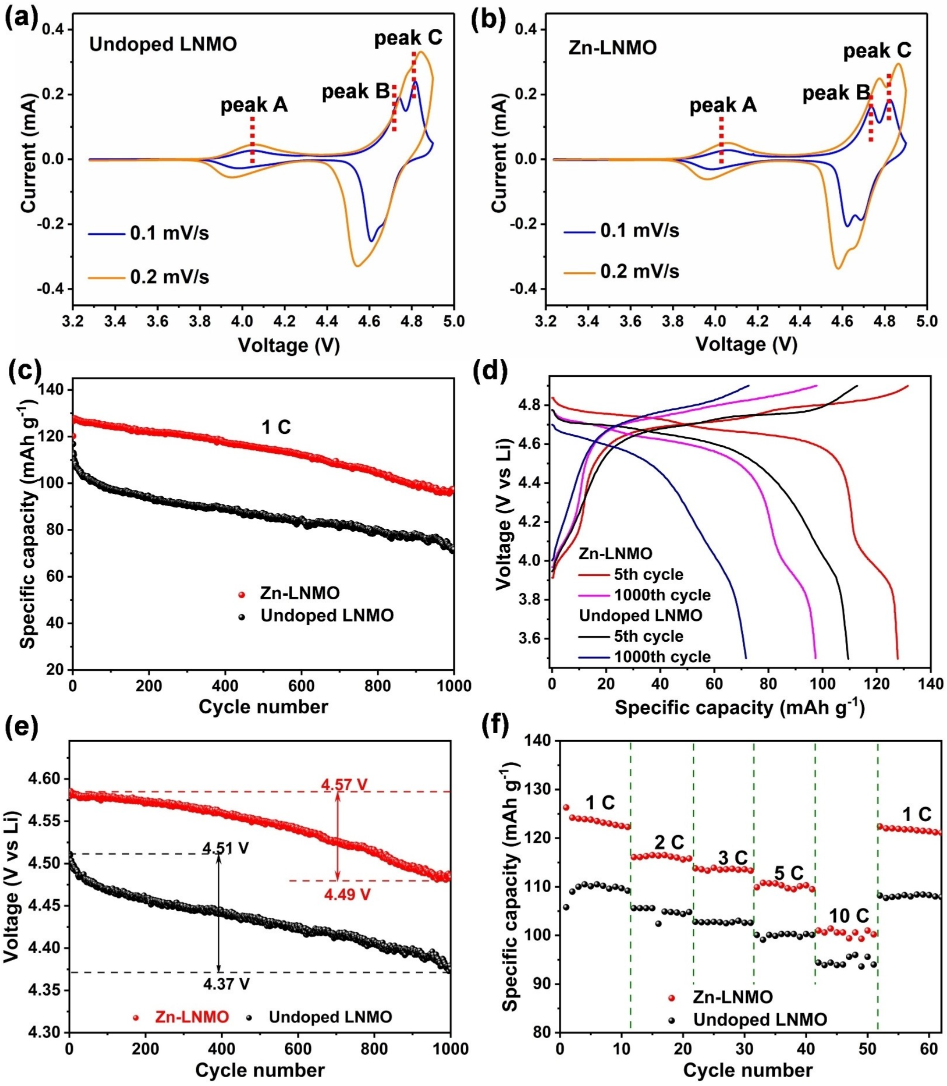

Figure 3. CV curves of (a) unmodified LNMO and (b) Zn-LNMO at different scan rates; (c) cycle performance of Zn-LNMO and unmodified LNMO at 1 C and (d) corresponding charge/discharge curves at the 5th and 1000th cycle; (e) average operating voltage (discharge energy density/ discharge battery capacity) and (f) rate capability of Zn-LNMO and unmodified LNMO.

corresponds to the redox couples Ni^{4+}/Ni^{3+} and Ni^{3+}/Ni^{2+}, with that at approximately 4.0 V associated with the Mn^{4+}/Mn^{3+} redox couple, consistent with our CV observations.[14] While the unmodified LNMO exhibits significant voltage polarization during cycling, the voltage polarization of Zn-LNMO is substantially suppressed, albeit with some degradation over extended cycling. The two-phase reaction above 4.8 V experienced by LNMO leads to the formation of the rock-salt type structured $Ni_{0.25}Mn_{0.75}O_2$ phase and loss of active cathode, resulting in voltage polarization that is avoided by the solid solution reaction of Zn-LNMO (Figure 2). Structurally, Zn resides at vacant 16*c* sites, serving to prevent the migration of Ni/Mn to adjacent 16*c* sites, eliminating the formation of the rock-salt type phase, and preventing structure degradation and suppressing voltage polarization. This insight into the influence of the Zn at 16*c* sites underscores the importance of understanding such structure-property effects in the strategic design of cathode materials. The higher discharge curve of Zn-LNMO compared with LNMO is attributable to the reduced voltage polarization, where voltage polarization is associated with the discharge voltage and energy density. During discharge, electrochemical reduction of Ni^{4+} to Ni^{3+} occurs at approximately 4.75 V, followed by further reduction of Ni^{3+} to Ni^{2+} at approximately ~4.65 V and reduction of Mn^{4+} to Mn^{3+} at approximately 4.0 V. Severe voltage polarization in the unmodified LNMO cathodes lowers the discharge voltage of all redox couples with consequential overlap between them. Figure 3d shows the voltage overlapping between the Ni^{3+}/Ni^{2+} and Mn^{4+}/Mn^{3+} redox couples, leading to a parabolic-type discharge curve for LNMO, with less evident ~4.65 V and ~4.0 V plateaus, in contrast to the three separate voltage plateaus exhibited during discharge by Zn-LNMO.

Figure 3e compares the average discharge voltage for both materials with the unmodified LNMO electrode rapidly dropping from 4.51 to 4.37 V over 1000 cycles, compared to the Zn-LNMO electrode that experienced a smaller decay from 4.57 to 4.49 V. The Zn-LNMO electrode exhibits better rate performance with capacity of 124, 116, 113, 110, and 101 mAh g^{-1} at 1 C, 2 C, 3 C, 5 C, and 10 C, respectively, compared to the unmodified LNMO that delivers 110, 105, 102, 100, and 94 mAh g^{-1}, respectively. Li diffuses within spinel-type structured LNMO by a jump diffusion mechanism from tetrahedral to octahedral to tetrahedral sites. The inclusion of Zn at only 5 % of 16*c* sites widens the smallest aperture of this channel by ~0.13 %, from 1.9530(3) to 1.9556(3) Å, as well as increasing the jump length between tetrahedral and octahedral sites from 1.77017(7) Å to 1.77204(7) Å, which both contribute to faster Li diffusion and improved rate performance (Figure 3f).

Post mortem NEXAFS analysis of Zn-LNMO and unmodified LNMO was performed in total electron yield mode to investigate the surface structure of materials. Figure 4a and 4c shows NEXAFS data at the Mn *L* edge for unmodified LNMO and Zn-LNMO at different states of charge, respectively. At OCV, the spectrum from both samples exhibits a peak characteristic of Mn^{4+}, with weaker peaks belonging to Mn^{3+}. However, at the fully charged state, the unmodified LNMO has a spectrum that is significantly different, with increases in the intensity of peaks characteristic of Mn^{2+} and Mn^{3+} and a decrease in the intensity of the peak characteristic of Mn^{4+}. This change in overall Mn valence in the unmodified LNMO may be associated with the phase transformation from the spinel-type to rock-salt type structured phases as observed in the SXRPD data. The observed valence reduction is consistent with the migration of Mn from 16*d* to 16*c* sites, as associated with Mn loss known to degrade battery performance. In comparison, the spectrum of Zn-LNMO is relatively unchanged at the fully charged state (Figure 4c), which is consistent with the SXRPD observation of a solid-solution reaction for the entire charge process. At the fully discharged state, both electrodes show increased intensity in peaks characteristic for Mn^{3+} and Mn^{2+}, which is related to the electrochemical reduction of Mn at approximately 4.0 V (Figure 3d), although Zn-LNMO has a lower ratio of Mn^{2+} to Mn^{4+} than the unmodified LNMO as a result of the absence of Mn^{2+} formation at high voltage. The spectrum for long-cycled Zn-LNMO is similar to that of the spectrum for Zn-LNMO after initial discharge, confirming enhanced structural stability. In contrast, the spectrum for long-cycled unmodified LNMO shows a significant drop in the intensity of peaks characteristic for Mn^{2+} and Mn^{3+} compared to the spectrum after the initial discharge, revealing substantial dissolution of Mn and loss from the structure, while the intensity of the peak arising from Mn^{4+} is relatively unaffected.

Figure 4b and 4d show the O *K* edge NEXAFS data of both samples at different states of charge. Peak A relates to the combination of spin-down t_{2g} and spin-up e_g states, while peak B corresponds to spin-down e_g states.[15] Considering the electronic configuration of Ni and Mn in LNMO (Mn^{3+}: $t_{2g}^4e_g^0$; Mn^{4+}: $t_{2g}^3e_g^0$; Ni^{2+}: $t_{2g}^6e_g^2$), peak A is assigned to the interaction between Mn 3*d* and O 2*p* orbitals and peak B is associated with the hybridization between Ni 3*d* and O 2*p* orbitals. Peak C is a fingerprint for carbonate species of the solid electrolyte interphase (SEI).[11] During charge, peaks A and B in both samples undergo substantial changes, with peak A decreasing in intensity and peak B increasing in intensity. Compared with Mn^{4+}, Mn^{3+} has less available space for the spin-down states of activated oxygen electrons, and the reduction of Mn^{4+} to Mn^{3+} therefore decreases the intensity of peak A. Disproportion of unstable Mn^{3+} leads to the formation of Mn^{4+} and electrolyte-soluble Mn^{2+}, and therefore, the intensity decrease of peak A can be linked to the dissolution of Mn. Oxidation of Ni leads to the loss of e_g electron orbitals, requiring additional activated oxygen electrons to fill spin-down e_g states, increasing energy absorption and the intensity of peak B. At the end of the discharge, peaks A and B in both samples exhibit notable changes, signalling irreversible reactions. After 50 cycles, the spectrum of the unmodified LNMO exhibits an increased intensity of peak C, consistent with the formation of a thick SEI layer that typically leads to slower insertion and extraction of Li. In contrast, peak C following initial discharge of Zn-LNMO is relatively unchanged after long-cycling. In summary, the inclusion of Zn at 16*c* sites both reduced the dissolution of Mn from the LNMO structure and the formation of a thick SEI. Despite these changes advantageous for battery performance, substantial changes in the state of both Mn and O known

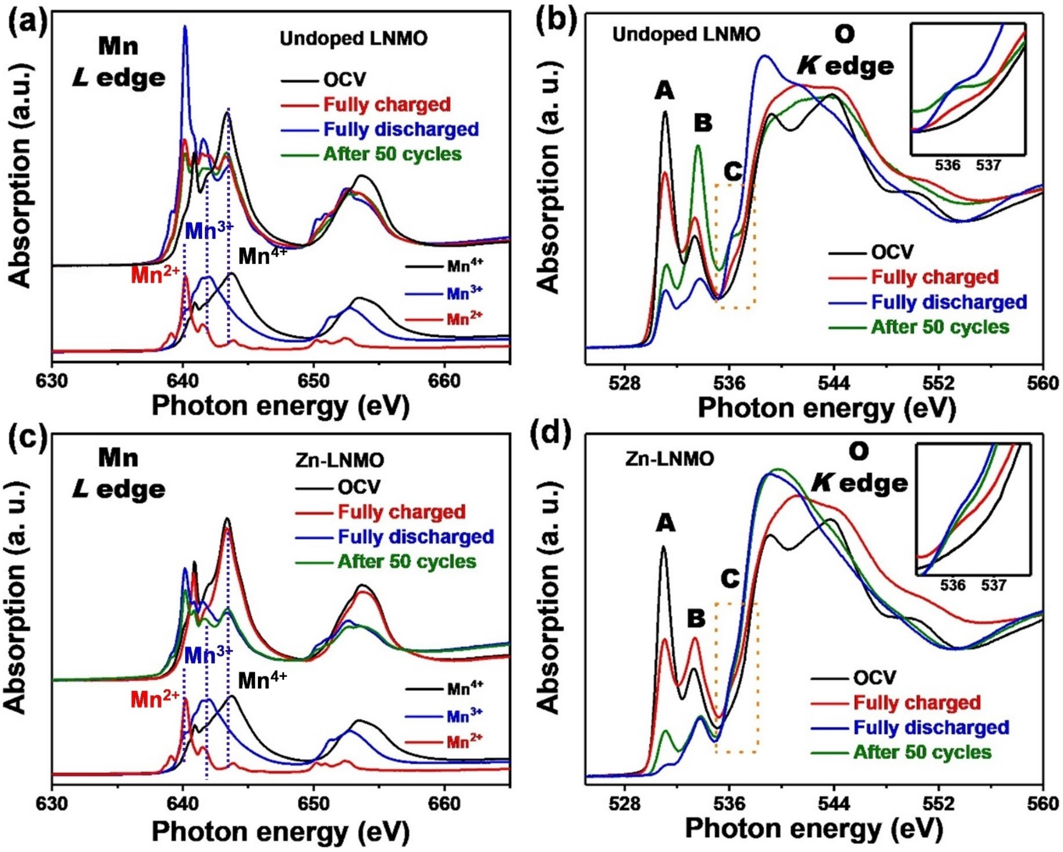

Figure 4. Mn *L* edge NEXAFS data of (a) unmodified LNMO and (c) Zn-LNMO at different states of charge, with the spectra for Mn-containing reference materials shown at the bottom and offset in y for clarity; O *K* edge NEXAFS spectra of (b) unmodified LNMO and (d) Zn-LNMO at different states of charge. The inset shows the details of Peak C.

detrimental for battery performance in both samples highlight the remaining need to understand the detailed influence of structure modification on electrode behavior to guide materials development towards stable battery performance.

Conclusions

We investigated the structure-function relationship of high-voltage $LiNi_{0.5}Mn_{1.5}O_4$ (LNMO) cathodes with Zn at previously vacant octahedral 16*c* sites in the spinel-type crystal structure with $Fd\bar{3}m$ space group symmetry. Our results show that Zn at 16*c* sites acts as structurally-stabilizing pillars, mitigating the two-phase reaction that occurs at high voltage that is responsible for rapid capacity decay. Consequently, batteries containing the Zn modified LNMO electrode exhibit improved cycle stability and enhanced rate performance compared to unmodified LNMO. We find that the addition of Zn at 16*c* sites does not address entirely the problems of voltage polarization, or loss of Mn or O from the structure upon extended cycling. This work underscores the critical role of understanding the fundamental structure-function relationship in driving battery materials development and offers insight for the design of high-performance, high-voltage spinel lithium-ion battery cathodes.

Acknowledgements

This work is supported by the Australian Research Council (FL210100050) and Australia's Economic Accelerator Seed Program (Grant Number AE230100120). This research was also supported by an AINSE Ltd. Early Career Researcher Grant (ECRG- G. Liang). Part of this work was carried out at the Powder Diffraction beamline (M20500), the Soft X-ray (SXR) beamline (M20609, M21238) of the Australian Synchrotron, and the Echidna instrument (P14124) at the Australian Centre for Neutron Scattering at the Australian Nuclear Science and Technology Organisation (ANSTO). Open Access publishing facilitated by Australian Nuclear Science and Technology Organisation, as part of the Wiley - Australian Nuclear Science and Technology Organisation agreement via the Council of Australian University Librarians.

Conflict of Interests

The authors declare no conflict of interest.

Data Availability Statement

The data that support the findings of this study are available from the corresponding author upon reasonable request.

Keywords: lithium-ion batteries · high-voltage spinel cathodes · structure function relation · octahedral interstitial site · site-specific doping

[1] a) W. Li, E. M. Erickson, A. Manthiram, *Nat. Energy* **2020**, *5*, 26–34; b) A. Konarov, S.-T. Myung, Y.-K. Sun, *ACS Energy Lett.* **2017**, *2*, 703–708.

[2] a) G. Liang, V. K. Peterson, K. W. See, Z. Guo, W. K. Pang, *J. Mater. Chem. A* **2020**, *8*, 15373–15398; b) T. Fu, D. Lu, Z. Yao, Y. Li, C. Luo, T. Yang, S. Liu, Y. Chen, Q. Guo, C. Zheng, *J. Mater. Chem. A* **2023**, *11*, 13889–13915.

[3] A. Manthiram, K. Chemelewski, E.-S. Lee, *Energy Environ. Sci.* **2014**, *7*, 1339.

[4] a) W. K. Pang, N. Sharma, V. K. Peterson, J.-J. Shiu, S.-h. Wu, *J. Power Sources* **2014**, *246*, 464–472; b) T. Tian, L.-L. Lu, Y.-C. Yin, Y.-H. Tan, T.-W. Zhang, F. Li, H.-B. Yao, *Small* **2022**, *18*, 2106898.

[5] a) G. Liang, A. S. Pillai, V. K. Peterson, K.-Y. Ko, C.-M. Chang, C.-Z. Lu, C.-E. Liu, S.-C. Liao, J.-M. Chen, Z. Guo, W. K. Pang, *Front. Energy Res.* **2018**, *6*, 89; b) G. Liang, C. Didier, Z. Guo, W. K. Pang, V. K. Peterson, *Adv. Mater.* **2020**, *32*, e1904528.

[6] a) B. Zong, Y. Lang, S. Yan, Z. Deng, J. Gong, J. Guo, L. Wang, G. Liang, *Mater. Today Commun.* **2020**, *24*, 101003; b) G. Liu, J. Zhang, X. Zhang, Y. Du, K. Zhang, G. Li, H. Yu, C. Li, Z. Li, Q. Sun, *J. Alloys Compd.* **2017**, *725*, 580–586.

[7] a) G. Liang, Z. Wu, C. Didier, W. Zhang, J. Cuan, B. Li, K. Y. Ko, P. Y. Hung, C. Z. Lu, Y. Chen, G. Leniec, S. M. Kaczmarek, B. Johannessen, L. Thomsen, V. K. Peterson, W. K. Pang, Z. Guo, *Angew. Chem. Int. Ed.* **2020**, *59*, 10594–10602; b) G. Liang, V. K. Peterson, Z. Wu, S. Zhang, J. Hao, C. Z. Lu, C. H. Chuang, J. F. Lee, J. Liu, G. Leniec, S. M. Kaczmarek, A. M. D'Angelo, B. Johannessen, L. Thomsen, W. K. Pang, Z. Guo, *Adv. Mater.* **2021**, e2101413; c) G. Liang, E. Olsson, J. Zou, Z. Wu, J. Li, C. Z. Lu, A. M. D'Angelo, B. Johannessen, L. Thomsen, B. Cowie, V. K. Peterson, Q. Cai, W. K. Pang, Z. Guo, *Angew. Chem. Int. Ed.* **2022**, *61*, e202201969.

[8] J.-Y. Piao, Y.-G. Sun, S.-Y. Duan, A.-M. Cao, X.-L. Wang, R.-J. Xiao, X.-Q. Yu, Y. Gong, L. Gu, Y. Li, Z.-J. Liu, Z.-Q. Peng, R.-M. Qiao, W.-L. Yang, X.-Q. Yang, J. B. Goodenough, L.-J. Wan, *Chem* **2018**, *4*, 1685–1695.

[9] R. D. Shannon, *Acta Crystallogr.* **1976**, *32*, 751–767.

[10] M. Lin, L. Ben, Y. Sun, H. Wang, Z. Yang, L. Gu, X. Yu, X.-Q. Yang, H. Zhao, R. Yu, M. Armand, X. Huang, *Chem. Mater.* **2014**, *27*, 292–303.

[11] B. Xiao, H. Liu, J. Liu, Q. Sun, B. Wang, K. Kaliyappan, Y. Zhao, M. N. Banis, Y. Liu, R. Li, T. K. Sham, G. A. Botton, M. Cai, X. Sun, *Adv. Mater.* **2017**, *29*, 1703764.

[12] a) A. Kraytsberg, Y. Ein-Eli, *Adv. Energy Mater.* **2012**, *2*, 922–939; b) W. K. Pang, H.-F. Lin, V. K. Peterson, C.-Z. Lu, C.-E. Liu, S.-C. Liao, J.-M. Chen, *J. Phys. Chem. C* **2017**, *121*, 3680–3689; c) J.-H. Kim, S.-T. Myung, C. Yoon, S. Kang, Y.-K. Sun, *Chem. Mater.* **2004**, *16*, 906–914.

[13] H. Lin, Y. Zhang, J. Hu, Y. Wang, L. Xing, M. Xu, X. Li, W. Li, *J. Power Sources* **2014**, *257*, 37–44.

[14] X. Ji, X. Dai, F. Wu, H. Jin, *ACS Sustainable Chem. Eng.* **2022**, *10*, 9850–9859.

[15] Y. Fan, E. Olsson, G. Liang, Z. Wang, A. M. D'Angelo, B. Johannessen, L. Thomsen, B. Cowie, J. Li, F. Zhang, *Angew. Chem. Int. Ed.* **2023**, *62*, e202213806.

Manuscript received: February 28, 2024
Revised manuscript received: April 15, 2024
Accepted manuscript online: May 1, 2024
Version of record online: June 20, 2024